



Available online at [www.sciencedirect.com](http://www.sciencedirect.com)  
**jmr&t**  
 Journal of Materials Research and Technology  
 journal homepage: [www.elsevier.com/locate/jmrt](http://www.elsevier.com/locate/jmrt)



## Original Article

# Quantitative prediction of yield strength of highly alloyed complex steel using high energy synchrotron X-ray diffractometry



Sumit Ghosh <sup>a,b,1</sup>, Shubo Wang <sup>a,c,1</sup>, Harishchandra Singh <sup>a,c,\*</sup>,  
 Graham King <sup>d</sup>, Yi Xiong <sup>e,f,\*\*</sup>, Tian Zhou <sup>f</sup>, Marko Huttula <sup>a,c,e</sup>,  
 Jukka Kömi <sup>a,b</sup>, Wei Cao <sup>a,c</sup>

<sup>a</sup> Centre for Advanced Steels Research, University of Oulu, FIN-90014, Finland

<sup>b</sup> Materials and Mechanical Engineering, University of Oulu, FIN-90014, Finland

<sup>c</sup> Nano and Molecular Systems Research Unit, University of Oulu, FIN-90014, Finland

<sup>d</sup> Canadian Light Source, 44 Innovation Blvd., Saskatoon, Saskatchewan S7N 2V3, Canada

<sup>e</sup> School of Materials Science and Engineering, Henan University of Science and Technology, Luoyang, 471023, Henan, China

<sup>f</sup> Collaborative Innovation Center of Nonferrous Metals, Luoyang, 471023, Henan, China

## ARTICLE INFO

### Article history:

Received 30 March 2022

Accepted 10 July 2022

Available online 16 July 2022

### Keywords:

Super-duplex stainless steel

Synchrotron radiation

High energy synchrotron X-ray diffraction

Analytical model

Yield strength

Cold- and cryogenic-deformation

## ABSTRACT

The overwhelming impact of complex-phase microstructures to mechanical response in multiphase steels requires accurate constitutive properties of the individual phases. However, precise prediction of individual phase properties to their mechanical response is critical and sophisticated, and commonly requires multiscale characterizations and numerous approximations. In this work, by employing full phase information and semi-empirical analytical models, we accurately predict the yield strength of deformed variants of Ce-modified SAF2507 super duplex stainless steel (SDSS). High energy synchrotron X-ray diffraction (HE-SXRD) reveals the phase fractions of major phases along with secondary phases of Cr<sub>2</sub>N and eutectic Ce<sub>x</sub>Fe<sub>y</sub>. Average lattice strain/crystallite size of the austenite and ferrite/martensite phases from the measured volume is estimated through the Williamson-Hall method. A unique composite strengthening type analytical model is used to estimate yield strength by taking individual strengthening contributions from all phases, their grain sizes, stored dislocation densities, solid solution, and precipitates. Close agreement between reconstructed and experimental yield strength is observed for several cold and cryogenic rolled SDSS. A combination of HE-SXRD and analytical model offers a time-effective virtual design pathway to engineer high-strength steel.

© 2022 The Author(s). Published by Elsevier B.V. This is an open access article under the CC BY-NC-ND license (<http://creativecommons.org/licenses/by-nc-nd/4.0/>).

\* Corresponding author.

\*\* Corresponding author.

E-mail addresses: [harishchandra.singh@oulu.fi](mailto:harishchandra.singh@oulu.fi) (H. Singh), [xiongy@haust.edu.cn](mailto:xiongy@haust.edu.cn) (Y. Xiong).

<sup>1</sup> Equal contribution authors.

<https://doi.org/10.1016/j.jmrt.2022.07.066>

2238-7854/© 2022 The Author(s). Published by Elsevier B.V. This is an open access article under the CC BY-NC-ND license (<http://creativecommons.org/licenses/by-nc-nd/4.0/>).

## 1. Introduction

The macro-mechanical response of a typical material such as steel is mainly determined by individual constitutive properties of microconstituents present within the material, their crystal structure/size, defect/dislocation density, etc. Application of external load through plastic deformation further perturb the microstructure significantly and thereby influence the mechanical property to a great extent. Super duplex stainless steel (SDSS), an imperative variant of highly alloyed structural and engineering materials, has constantly been developed to meet the requirement of high strength and toughness combination along with better wear resistance [1]. Nevertheless, investigation of the underlying property of such SDSS is complicated due to the intrinsic heterogeneous microstructures leading to a different response to various deformations. Large varieties, compositions, and distributions of alloying elements within SDSS further complicate the in-depth studies of the respective mechanism. These hurdles drive a need for the advanced suitable probe and methodology for engineering high strength steel employing the time-effective approach.

The virtual prediction concept simplifies and economizes making routes of structural materials which typically involve technical and engineering sophistication. For example, to characterize the accommodation of loading stresses among different phases the governing micro mechanisms associated during the elastic–plastic deformation of dual/multi-phase steels, several micromechanical models were used through estimating stress/strain between different phases. Jia et al. [2,3] and Cong et al. [4] studied the evolution of lattice strains and load partitioning of dual phase (DP) and transformation induced plasticity (TRIP) assisted steels using the HE-SXRD technique. They have developed a visco-plastic self-consistent (VPSC) model for two/multi-phase materials to simulate the micromechanical behavior of the steels [2–4]. Fu et al. [5] proposed an analytical model to characterize not only the phase-to-phase stress interaction but also the change in the work-hardening rate of each phase during plastic flow. The proposed analytical model can be easily combined with a few numerical simulation codes, such as the finite element method (FEM), for predicting manufacturing processes and service lives of engineering components of advanced steels with complex multi-scale microstructures [5,6]. However, the successful implementation of several proposed semi-empirical analytical models to explain the observed mechanical performances requires complete structural details [7,8], which needs numerous characterization techniques and approximations of models. Furthermore, the prediction of mechanical properties for a single-phase or even bi-phasic alloy has been realized, however, the same for multiphase steel is elusive due to difficulty in observing its complex microstructure through the conventional approach.

Moreover, determining mechanical properties, for example, the yield strength (YS) by a tensile test is simple, however, the estimation of individual strengthening contributions requires multiscale microstructural characterizations. Various characterization techniques such as scanning electron microscopy, electron backscatter diffraction, transmission electron microscopy (TEM), lab source X-ray diffraction (LS-XRD), and atom-probe tomography [9–12] have been employed to obtain necessary microstructural details, which however is time-consuming. For example, dislocation density, a crucial factor influencing the YS, can be determined by TEM [13], however, it is difficult to estimate accurately from severely deformed material containing dense dislocation substructures due to complicated image contrasts [14]. In addition, only a shallow volume near the surface can be investigated by aforesaid multiscale techniques, lacking microstructural statistics from the bulk. Such an expensive strategy can be avoided prior to designing/engineering high strength steel through the recent advancement in Synchrotron Radiation (SR)-based methods, for example, high energy synchrotron X-ray diffraction (HE-SXRD) [6,15,16], successfully revealing the hidden structural information and its relationship to properties, performance, processing, and environment.

SR empowered HE-SXRD offers a non-invasive method for studying the structure and penetrates deeply into materials to statistically quantify and estimate the microstructural features in steel [17–19]. In addition to the phase fraction determination, XRD profile analysis using Williamson–Hall (W–H) method offers an alternative route to estimate not only dislocation densities, crystallite size, and lattice microstrain, but also enable the prediction of YS of a bulk highly alloyed and deformed bulk steel through an analytical model.

In this work, we present precise calculations of YS solely by employing HE-SXRD on several cold- and cryogenic-rolled Ce-modified SDSS. By implementing the W–H method on HE-SXRD data, this work elucidates the microconstituents and their individual contribution to predict YS. Taking individual strengthening contributions from all phases, their grain sizes, stored dislocation densities, solid solution and precipitates, YS is estimated through a unique composite strengthening type analytical model. Such evaluation of strengthening contributions through an analytical model could be a rapid verification method for the design of high-strength steel by optimizing strengthening contributions and tailoring the microstructures. Moreover, this work benefits the idea of prediction of YS for highly alloyed complex SDSS.

## 2. Experimental

The selected material for the present study is Ce-modified SDSS (Ce-SAF2507) with a nominal composition listed in

**Table 1 – Chemical composition of the test material (wt. %).**

C	Si	Mn	P	S	Cr	Ni	Mo	N	Ce	Fe
0.023	0.35	0.8	≤0.03	≤0.03	25	5.4	3.4	0.5	0.08	Bal.

**Table 1.** Details about the processing details can be found in our other works [20–22]. The Ce-SAF2507 plates were solid-solution treated at 1050 °C for 2 h followed by water quenched to room temperature. The solid solution treated plates were subjected to room temperature cold rolling (CR) and cryogenic rolling (CGR) in liquid nitrogen (at  $\sim -196$  °C) to achieve  $\sim 30$ , 50, 70, and 90% thickness reduction (an equivalent true strain of 0.4, 0.7, 1.2, and 2.3, respectively) with a strain rate of  $10^{-2}$  s $^{-1}$ .

Lab source (LS)-XRD measurements were performed using a Cu–K  $\alpha$  radiation (Bruker D8). For HE-SXRD measurements, rectangular blocks of SDSS with a dimension of  $1 \times 1 \times 1.5$  mm $^3$  were measured at the Brockhouse High Energy Wiggler Beamline, Canadian Light Source, Canada. The samples were mounted to the sample stage with the normal direction (ND) parallel to the beam, the rolling direction (RD) parallel to the horizontal direction. No sample rotation was applied during data acquisition. Slits in front of the sample were used to

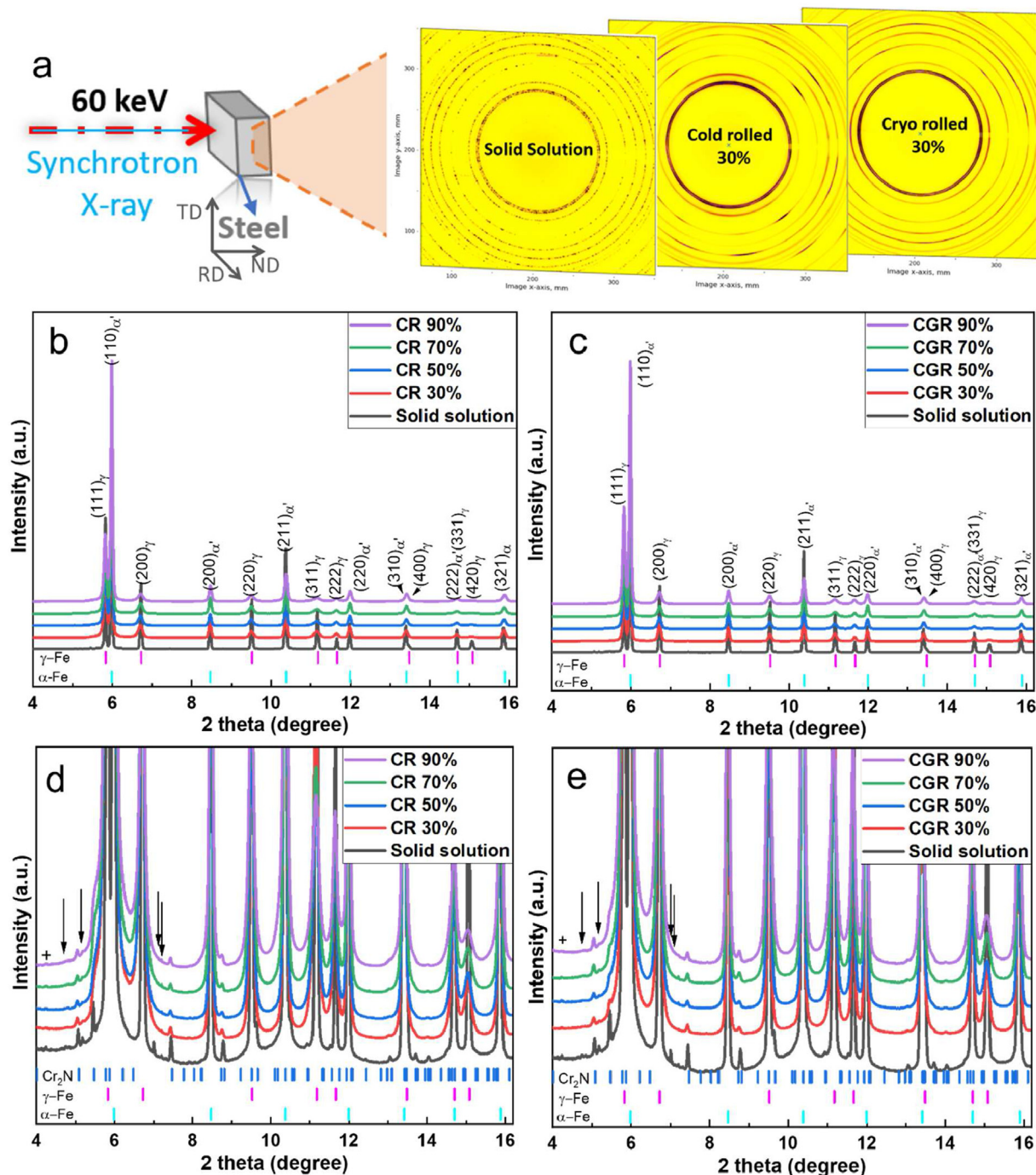


**Fig. 1** – (a) Schematic illustration of the HE-SXRD experiment; HE-SXRD 1D profiles obtained from the (b) CR, and (c) CGR SDSS specimens, respectively. (d) and (e) are the magnified figure of (b) and (c), respectively.



define a  $200\ \mu\text{m} \times 300\ \mu\text{m}$  beam size through the sample, giving a  $0.09\ \text{mm}^3$  illuminated volume. The data were collected in transmission mode (Fig. 1a) with 60 keV photons. The refined wavelength from a  $\text{LaB}_6$  calibrant was  $\lambda = 0.212561\ \text{\AA}$ , and the sample to detector distance was 740 mm. An exposure time of

0.3 s was used along with 120 frames for each of these data collections using a PerkinElmer area detector, a flat panel X-ray detector,  $200\ \mu\text{m}$  pixel,  $40 \times 40\ \text{cm}^2$ . The obtained raw 2D diffraction patterns (Fig. 1a) were integrated into 1D diffractograms by the GSAS-II software [23]. Quantitative

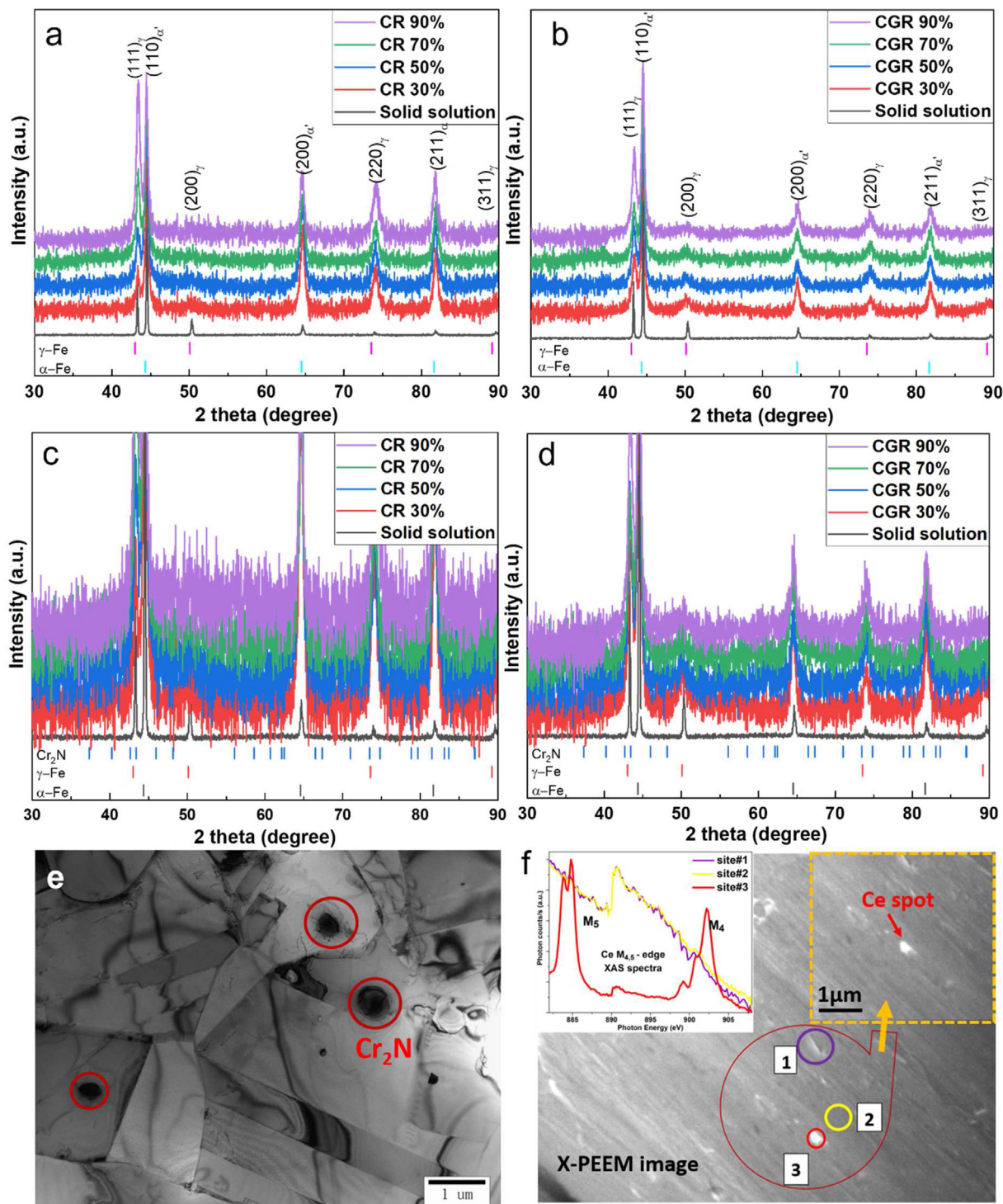


Fig. 2 – Lab-source XRD patterns obtained from (a) CR and (b) CGR SDSS specimens, respectively; (c), (d) show magnified view of (a) and (b), respectively; (e) TEM bright field image showing the presence of nanoscale  $\text{Cr}_2\text{N}$  precipitates in the SDSS specimens, reproduced from [14]; and (f) X-PEEM image and XAS spectra crossing Ce  $M_{4,5}$  edge at various spatial positions as marked in the image. Inset of (f) shows the enlarged image of associated Ce spot, reproduced from [37].

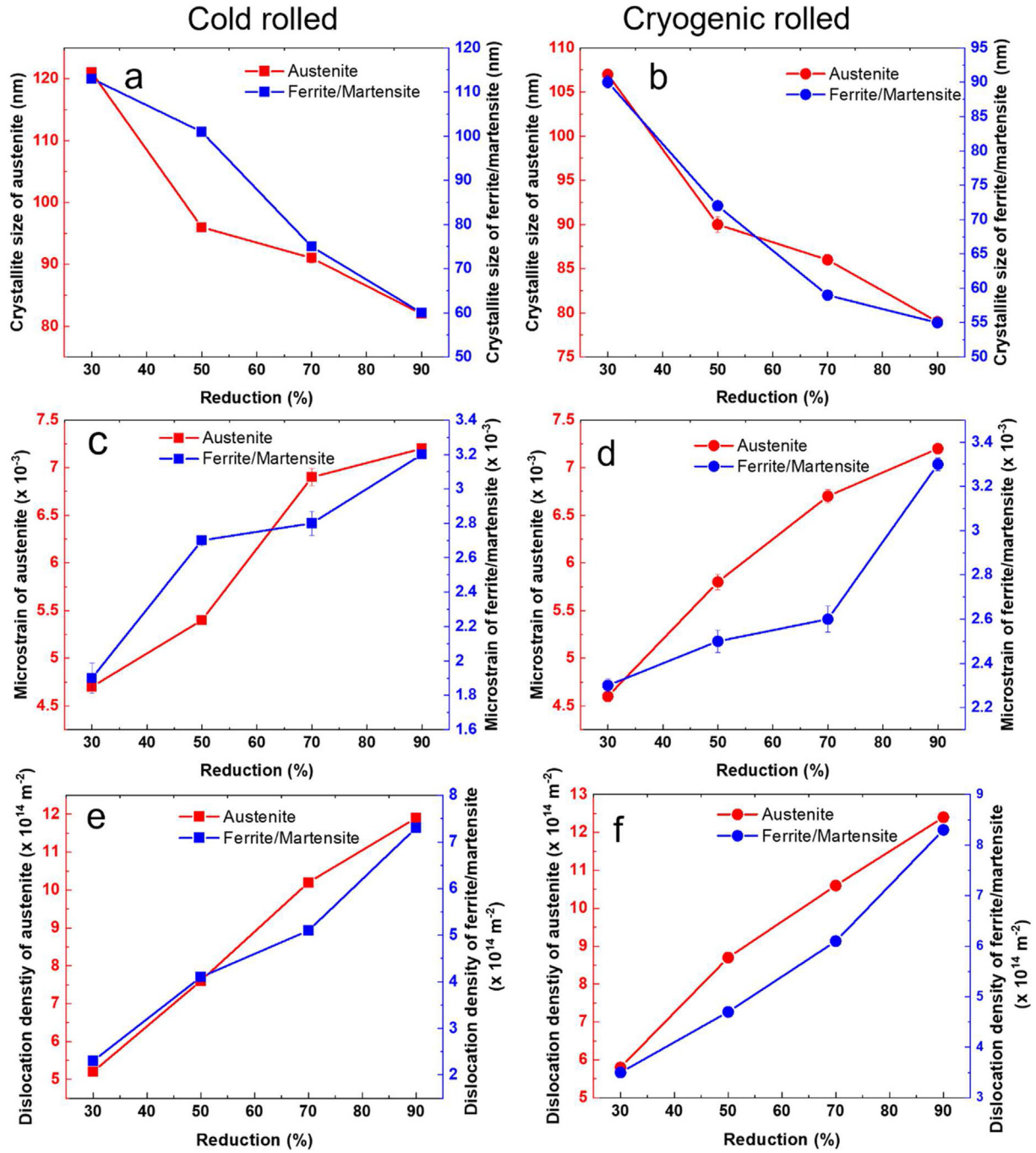


Fig. 3 – (a, b) Crystallite size, (c, d) microstrain, and (e, f) dislocation density of the austenite and ferrite/martensite phases in the SDSS specimens after CR and CGR, respectively. In most cases, the error bars are within the symbol.

analysis using Rietveld refinement was carried out using the Match software [24].

For microstructural analysis, a corresponding peak profile from the original solid solution sample has been used to eliminate the instrumental peak broadening to calculate the broadening due to microstrain (root-mean-square strain) and crystallite size averaged over the diffracting volume. Here, the solid solution sample is regarded to be ‘strain-free’, which is not the case as the solutes could distort the lattice. Therefore, following determined dislocation densities and crystallite size

in this work are relative values to the referenced solid solution sample attributed mainly to CR and CGR. The contribution of which to the total broadening has been estimated as follows [25]:

$$\beta_r = \sqrt{(\beta_{obs}^2 - \beta_i^2)} \quad (1)$$

where  $\beta_r$  is the total broadening due to the microstrain and crystallite size,  $\beta_i$  and  $\beta_{obs}$  are the integral breadth at the full width at half maxima (FWHM) of the fitted Gaussian shape

peaks for the solid solution and deformed specimens, respectively. For separating the contribution from microstrain and crystallite size, the simplistic W–H method is used, wherein, the average peak broadening of seven peaks of each specimen has been accounted by plotting  $\beta_r \cos \theta$  vs.  $\sin \theta$ . The observed line breadth is a sum of two terms:

$$\beta_r = 0.9\lambda/\tau \cos \theta + 4\varepsilon \tan \theta \quad (2)$$

where  $\lambda$  is the wavelength,  $\theta$  is the Bragg angle,  $\tau$  is the crystallite size, and  $\varepsilon$  is the microstrain.

The average crystallite size is given by

$$\tau = 0.9\lambda/\beta_r \cos \theta \quad (3)$$

while the microstrain is

$$\varepsilon = \beta_r/4 \tan \theta \quad (4)$$

The dislocation density ( $\rho_d$ ) is estimated from the average  $\tau$  and  $\varepsilon$  as follow [26]:

$$\rho_d = \frac{2\sqrt{3}}{b} \frac{\varepsilon^{2/2}}{\tau} \quad (5)$$

where,  $b$  the Burgers vector, is ~0.249 and 0.254 nm for ferrite/martensite and austenite [27,28].

### 3. Results and discussions

Fig. 1 and Fig. 2 depict the HE-SXRD and LS-XRD patterns of SDSS specimens along with 2D images from the SR data. Clear differences in the relative intensities of various peaks for the two different sources are apparent. Compared to the LS-XRD, HE-SXRD data typically suggests a few differences for all the deformed samples: i) relative intensity of peaks corresponding to ferrite/martensite ( $\alpha/\alpha'$ ) and austenite ( $\gamma$ ) phase, an indication of a difference in the phase fractions; ii) observation of several additional peaks which are not visible with lab-source (Fig. 1d,e vs. Fig. 3). The observed differences in phase fractions, estimated by Rietveld refinement implemented in GSAS II [23], can be attributed to the difference in the phase fraction

at the surface and bulk (Table 2 vs. Table 3). Such differences can be because rolling gives different phases and texture components through the thickness or along the ND [29,30]. LS-XRD only probes microstructures within a few hundreds of  $\mu\text{m}$  into the specimens, the SR, on the other hand, can penetrate the entire 1.5 mm thick steel plates, detect the phases within the bulk and give better statistics. Further, observation of additional peaks with HE-SXRD is attributed to the usage of SR with high photon flux, high brilliance and low divergence providing high penetration depth into the material (large analysed volume) and low-noise detector [31,32]. Such a comparison of LS vs. SR source clearly demonstrates the importance of using HE-SXRD to reveal the difference in phase fraction in bulk and surface along with additional minor crystalline phases.

By excluding the peak (marked by '+' in Fig. 1d and e) corresponding to the second harmonic, the additional relatively weak new crystalline peaks in the HE-SXRD patterns can be attributed to  $\text{Cr}_2\text{N}$  precipitates (Fig. 1). The formation of  $\text{Cr}_2\text{N}$  secondary phase, as illustrated in Fig. 2e, is ascribed to the addition of N element, which substitutes the expensive Ni content, making the SDSS more cost-effective [33]. The diffraction peaks of  $\text{Cr}_2\text{N}$  overlap with peaks of ferrite and austenite, which could be the reason for the emergence of shoulder peaks in the HE-SXRD patterns. The phase fraction (wt.%) of  $\text{Cr}_2\text{N}$ , determined by HE-SXRD data (Table 2), is quite low that cannot be detected by LS-XRD. Further, the extra hidden minor peaks agree with the  $\text{Ce}_x\text{Fe}_y$  phases, as shown by arrows in Fig. 1d, e. In general, Ce or other rare earth (RE) elements is added to purify molten steel and modify the inclusions [34], which could form solid solution, inclusions, and/or secondary phases, such as RE-Fe(-P) eutectic phase and Fe-RE intermetallic compounds [35]. These results also match the observation of RE clustering phase in one of the CR samples obtained through X-PEEM [36], as also reproduced in Fig. 2f [37].

Following the phase fraction determination, the microstructural details such as crystallite size, microstrain and dislocation density, are estimated through a simple W–H method considering the average peak broadening of seven peaks both for austenite and ferrite/martensite of each condition, are summarized in Fig. 3 and Table 4. The width of the

**Table 2 – Fractions of phases within the SDSS specimens determined by HE-SXRD profile analysis.  $R_{wp}$ : weighted profile residual obtained from Rietveld refinement is also included. In general, the deviation of fractions of  $\text{Cr}_2\text{N}$  in different samples is small, therefore, we use the median of fractions and average size of  $\text{Cr}_2\text{N}$ , taken as constants, to simplify the model for the predictions of YS.**

Sample	Phase fraction (wt.%)			$R_{wp}$
	Austenite	Ferrite/Martensite	$\text{Cr}_2\text{N}$	
Solid solution	43.3	52.9	3.8	7.737
CR 30%	34.1	62.2	3.7	8.998
CR 50%	31.1	65.3	3.6	8.276
CR 70%	29.3	67.2	3.5	9.320
CR 90%	26.3	70.4	3.3	7.874
CGR 30%	33.5	63.1	3.3	8.741
CGR 50%	31.4	65.3	3.3	8.389
CGR 70%	27.5	69.3	3.2	7.336
CGR 90%	33.0	63.7	3.3	8.660

**Table 3 – Fraction of phases within the steel specimens determined by LS-XRD profiles.  $R_{wp}$ : weighted profile residual obtained from Rietveld refinement is also included.**

Materials	Phase fraction (wt.%)		$R_{wp}$
	Austenite	Ferrite/Martensite	
Solid solution	30.8	69.2	9.451
CR 30%	23.8	76.2	9.366
CR 50%	29.4	70.6	8.467
CR 70%	39.1	60.9	9.643
CR 90%	48.8	51.2	9.844
CGR 30%	26.4	73.8	9.684
CGR 50%	26.3	73.9	8.984
CGR 70%	28.6	71.4	8.592
CGR 90%	33.5	66.5	9.467



**Table 4 – Quantitative microstructural features, i.e., grain size, microstrain, and dislocation density of the steel.**

Material	Crystallite Size (nm)		Microstrain ( $\times 10^{-3}$ )		Dislocation density ( $\times 10^{14} \text{ m}^{-2}$ )	
	$\gamma$	$\alpha$	$\gamma$	$\alpha$	$\gamma$	$\alpha$
CR 30%	121( $\pm 0.3$ )	113( $\pm 0.7$ )	4.7( $\pm 0.07$ )	1.9( $\pm 0.09$ )	5.2( $\pm 0.09$ )	2.3( $\pm 0.02$ )
CR 50%	96 ( $\pm 0.7$ )	101( $\pm 0.1$ )	5.4( $\pm 0.04$ )	2.7( $\pm 0.03$ )	7.6( $\pm 0.09$ )	4.1( $\pm 0.03$ )
CR 70%	91 ( $\pm 0.8$ )	75 ( $\pm 0.8$ )	6.9( $\pm 0.09$ )	2.8( $\pm 0.07$ )	10.2( $\pm 0.01$ )	5.1( $\pm 0.04$ )
CR 90%	82 ( $\pm 0.7$ )	60 ( $\pm 0.7$ )	7.2( $\pm 0.02$ )	3.2( $\pm 0.02$ )	11.9( $\pm 0.01$ )	7.3( $\pm 0.04$ )
CGR 30%	107( $\pm 0.1$ )	90 ( $\pm 0.9$ )	4.6( $\pm 0.06$ )	2.3( $\pm 0.03$ )	5.8( $\pm 0.06$ )	3.5( $\pm 0.02$ )
CGR 50%	90 ( $\pm 0.9$ )	72 ( $\pm 0.7$ )	5.8( $\pm 0.08$ )	2.5( $\pm 0.05$ )	8.7( $\pm 0.01$ )	4.7( $\pm 0.08$ )
CGR 70%	86 ( $\pm 0.6$ )	59 ( $\pm 0.1$ )	6.7( $\pm 0.07$ )	2.6( $\pm 0.06$ )	10.6( $\pm 0.01$ )	6.1( $\pm 0.02$ )
CGR 90%	79 ( $\pm 0.1$ )	55 ( $\pm 0.3$ )	7.2( $\pm 0.02$ )	3.3( $\pm 0.03$ )	12.4( $\pm 0.01$ )	8.3( $\pm 0.03$ )

peak steadily increases with an increase in the amount of reduction in both CR and CGR conditions. This is attributed to the increase in microstrain and the decrease in the crystallite size with an increased amount of thickness reduction from 30 to 90%. Overall, a relatively higher level of microstrain is noticed within austenite phase as compared to ferrite/martensite phase (Fig. 3a, b). This is due to the high strain hardening ability of austenite compared to ferrite/martensite [38]. With increasing thickness reduction during both CR/CGR, strain induced martensitic transformation occurred from metastable austenitic phase, resulting in a higher concentration of microstrain within austenite phase. In CR specimens, the average lattice microstrain in austenite increased from  $4.7 \times 10^{-3}$  to  $7.2 \times 10^{-3}$  and in martensite the same has increased from  $1.9 \times 10^{-3}$  and  $3.2 \times 10^{-3}$  with an increment in rolling reduction from 30 to 90% along with a concomitant decrease in the crystallite size from  $\sim 122$  to 82 nm and 113 to 61 nm (Fig. 3a, c), respectively. Similar trend was observed in the case of CGR specimens (Fig. 3b, d and Table 4). Accumulation of a large amount of microstrain in the austenite results in the formation of high-density dislocation substructures within the grains. The dislocation density in 90% rolled specimens was found to be markedly higher than that of the 30% rolled alloys (Fig. 3e, f). The observed non-monotonic behavior could be due to the simple W–H method applied in this study. Furthermore, these microstructural details are deployed to theoretically explore the YS of the selected steel, which is the primary focus of this work.

To estimate the overall contribution of both austenite and ferrite/martensite to the mechanical response, a composite strengthening model was applied [39]. The rule of mixtures was used to compute the yield of two primary phases as follows:

$$\sigma_y = \sum (v_\gamma \times \sigma_\gamma + v_\alpha \times \sigma_\alpha) \quad (6)$$

where  $v_\gamma$  and  $v_\alpha$  are the phase fraction of austenite ( $\gamma$ ) and ferrite/martensite ( $\alpha$ ) phases,  $\sigma_\gamma$  and  $\sigma_\alpha$  are the yield strength of  $\gamma$  and  $\alpha$  phases, respectively.

According to the Taylor hardening theory, the strengthening contribution from dislocations ( $\sigma_D$ ) can be estimated as follows [40,41]:

$$\sigma_D = aMGb\rho_d^{1/2} \quad (7)$$

where,  $M$  is the Taylor factor (3 for non-textured polycrystalline materials),  $G$  is the shear modulus (82 GPa) [27],  $a$

$\sim 0.3$  is a constant [42,43],  $b$  is the Burgers vector, and  $\rho_d$  is the dislocation density.

The grain sizes are significantly refined after CR and CGR (Fig. 3). The contribution of grain refinement to the overall strengthening can be given by [40]:

$$\sigma_H = \sigma_0 + K_H d^{-1/2} \quad (8)$$

where  $d$  is the average grain size and taken the same as  $\tau$  in Eq. (2), and  $K_H$  is the Hall-Petch (HP) constant.  $K_H$  is reported to be  $0.11\text{--}0.31 \text{ MN m}^{-3/2}$  [27,42,43]. In this study, we have taken this value as  $0.3 \text{ MN m}^{-3/2}$ . Furthermore, in order to calculate the grain size strengthening contribution, an appropriate definition of grain is important. Generally, HP relationship is valid with an average grain size of over  $1 \mu\text{m}$  and a negligible number of dislocations [40]. However, our previous studies showed evaluation of nano-size grains along with dense dislocation substructures in CR and CGR specimens [20,21]. Recently, Hasen et al. [40] reported that HP relationship derived from annealed or undeformed microstructure should be modified prior to extending in nanostructured materials containing high dislocation substructures. Therefore, based on the assumption of an identical strengthening mechanism, as recommended by Hasen et al. the relationship combining the HP and Taylor strengthening is considered by Eq. (9) as follows [40],

$$\sigma_{D+H} = \sigma_0 + \alpha G M b (\rho_D)^{1/2} + K_H d^{-1/2} \quad (9)$$

Other possible contributions are from solid solution strengthening and  $\text{Cr}_2\text{N/Ce}$  precipitation strengthening, which are assumed to distribute uniformly in the two phases and can be evaluated by Eqs. (10) [44] and (11) [45], respectively:

$$\sigma_{SS} = 0.686 \left[ 110(X_{Si}^{at})^{0.75} + 70(X_{Mn}^{at})^{0.75} + 61(X_{Ni}^{at})^{0.75} + 14(X_{Cr}^{at})^{0.75} \right] \quad (10)$$

where,  $X_i$  is the atomic concentration in wt.% of element  $i$  ( $i = \text{Si, Mn, Ni, Cr}$ ).

Precipitation strengthening can be attributed through shearing/bowing out between precipitates and cross slip/climb [45]. The hard particles increase the strength significantly by the Orowan strengthening mechanism and a critical size and incoherency of particle is required for an effective strengthening of the alloys [46]. The Ashby – Orowan relationship describes the effect of hard particles on the strengthening of alloys as follows [45–47]:

**Table 5 – Individual strengthening mechanism's contribution to YS and experimentally measured YS for CR and CGR SDSS.**  $\sigma_{SS}$ : strengthening contribution from solutes using Eq. (10);  $\sigma_P$ : strengthening contribution from secondary phase particles using Eq. (11); the fraction and average diameter of precipitates are taken as constants to simplify the calculation;  $\sigma_{D+H}$ : strengthening combining the HP and Taylor strengthening using Eq. (9);  $\sigma_Y$ :  $\Sigma$  RMS of overall strengthening combining the  $\sigma_{SS}$ ,  $\sigma_P$  and  $\sigma_{D+H}$ , predicted separately for primary  $\alpha$  and  $\gamma$  phases using Eq. (13);  $\sigma_y$ : composite strengthening model predicted YS using Eq. (6).

	$\sigma_{SS}$ (MPa)	$\sigma_P$ (MPa)	Phases	$\sigma_{D+H}$ (MPa)	$\sigma_Y$ (MPa)	$\sigma_y$ (MPa)
CR 30%	330( $\pm 0.7$ )	569 $\pm$ 0.5	$\gamma$	997( $\pm 0.7$ )	1195( $\pm 0.5$ )	1131( $\pm 0.7$ )
			$\alpha$	966( $\pm 0.4$ )	1169( $\pm 0.7$ )	
CR 50%	330 $\pm$ 0.7	569 $\pm$ 0.5	$\gamma$	1139( $\pm 0.3$ )	1316( $\pm 0.5$ )	1215( $\pm 0.6$ )
			$\alpha$	1053( $\pm 0.1$ )	1242( $\pm 0.3$ )	
CR 70%	330( $\pm 0.7$ )	569( $\pm 0.5$ )	$\gamma$	1199( $\pm 0.1$ )	1368( $\pm 0.7$ )	1320( $\pm 0.3$ )
			$\alpha$	1210( $\pm 0.5$ )	1378( $\pm 0.2$ )	
CR 90%	330( $\pm 0.7$ )	569( $\pm 0.5$ )	$\gamma$	1272( $\pm 0.4$ )	1432( $\pm 0.7$ )	1434( $\pm 0.3$ )
			$\alpha$	1366( $\pm 0.5$ )	1516( $\pm 0.9$ )	
CGR 30%	330( $\pm 0.7$ )	569( $\pm 0.5$ )	$\gamma$	1059( $\pm 0.6$ )	1247( $\pm 0.7$ )	1265( $\pm 0.2$ )
			$\alpha$	1091( $\pm 0.9$ )	1274( $\pm 0.9$ )	
CGR 50%	330( $\pm 0.7$ )	569( $\pm 0.5$ )	$\gamma$	1179( $\pm 0.5$ )	1350( $\pm 0.9$ )	1378( $\pm 0.1$ )
			$\alpha$	1227( $\pm 0.2$ )	1392( $\pm 0.2$ )	
CGR 70%	330( $\pm 0.7$ )	569( $\pm 0.5$ )	$\gamma$	1231( $\pm 0.7$ )	1396( $\pm 0.1$ )	1479( $\pm 0.6$ )
			$\alpha$	1364( $\pm 0.1$ )	1515( $\pm 0.4$ )	
CGR 90%	330( $\pm 0.7$ )	569( $\pm 0.5$ )	$\gamma$	1301( $\pm 0.7$ )	1458( $\pm 0.2$ )	1540( $\pm 0.5$ )
			$\alpha$	1436( $\pm 0.3$ )	1580( $\pm 0.3$ )	

$$\sigma_P = \left( \frac{0.538Gb\sqrt{f_P}}{d_P} \right) \ln \left( \frac{d_P}{2b} \right) \quad (11)$$

where  $G$  is the shear modulus (MPa),  $b$  is Burger's vector,  $d'$  is the diameter of the precipitates and  $f$  is the volume fraction of the precipitates. The average diameter of  $\text{Cr}_2\text{N}$  and  $\text{Ce}$  precipitates was estimated from TEM and PEEM investigation, as shown in Fig. 2e and f. Using Eq. (11) we have estimated the combined precipitation strengthening contribution due to  $\text{Cr}_2\text{N}$  and  $\text{Ce}$  as follows:

$$\sigma_P^{\text{Cr}_2\text{N}+\text{Ce}} = \left( \frac{K\sqrt{f_{\text{Cr}_2\text{N}}}}{d_{\text{Cr}_2\text{N}}} \right) \ln \left( \frac{d'_{\text{Cr}_2\text{N}}}{2b} \right) + \left( \frac{K'\sqrt{f_{\text{Ce}}}}{d'_{\text{Ce}}} \right) \ln \left( \frac{d'_{\text{Ce}}}{2b} \right) \quad (12)$$

where  $K$  and  $K'$  are the product of  $Gb$  for  $\text{Cr}_2\text{N}$  and  $\text{Ce}$ , respectively. In this work, the solutes, size and fractions of the precipitates are considered to be constant, i.e., the  $\sigma_{SS}$  and  $\sigma_P$  are constant in the CR and CGR samples to simplify the model. In combination with Eqs. (6–12), the overall YS can be calculated as follows:

$$\sigma_Y = \sqrt{\sigma_0^2 + \sigma_{SS}^2 + \sigma_P^2 + \sigma_{D+H}^2} \quad (13)$$

where, ' $\sigma_0$ ' is flow stress (for austenite,  $\sigma_0 = 25$  MPa, and for martensite/ferrite  $\sigma_0 = 30$  MPa [48,49]).

Table 5 lists the contribution of different strengthening mechanisms to the overall YS. The difference between the experimental (Fig. 4) and predicted values of the overall YS is insignificant (Fig. 5), where these data fluctuate near a straight line with a slope of one, and the deviation is less than 10%. This proves the rationality of the current prediction via microconstituents determination using HE-SXRD and analytic models. The observed small difference between the calculated and measured values could be due to the most simplistic W–H method used here. Simple W–H method ignores the effect of the dislocation arrangement and the dislocation contrast

factors, i.e., the strain anisotropy, which is displayed in the non-monotonic behavior of the W–H plots (Fig. 3). Such dislocation arrangement and density together define the microstrain in the lattice. A few possible improvements have recently been suggested via the modified W–H approach and full pattern fitting methods [48], which is not within the scope of the present study. Moreover, XRD data do not provide information on deformation twin density and other defects [50]. Further, the current SDSS is modeled as isotropic, which is highly unlikely in practice and thus might be contributing to the discrepancy in the predicted and experimental YS values. However, it is interesting to note that even a simple W–H

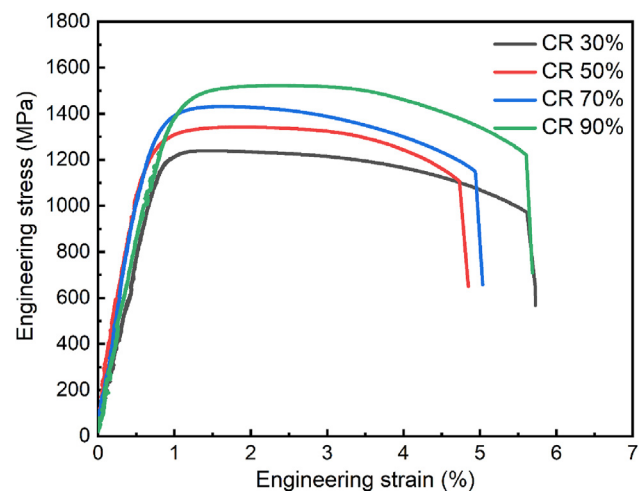


**Fig. 4 – Representative engineering stress vs. strain curve of the CR SDSS samples. Corresponding extracted yield strength values are given in [12] for CR samples [13] for CGR samples.**



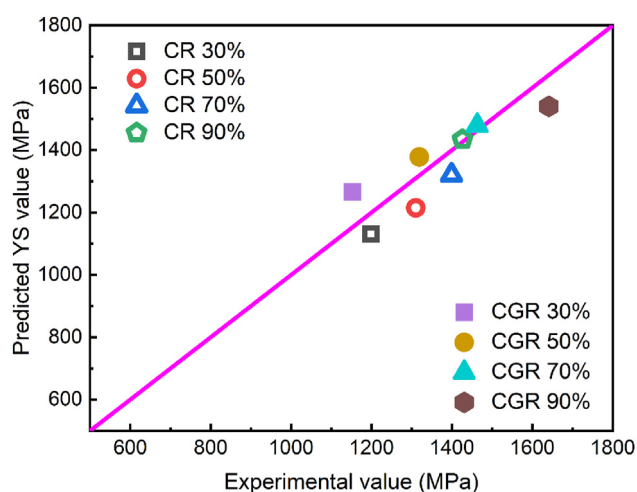


**Fig. 5 – The summary of predicted and experimental YS values. Experimental values are extracted from [12–14], and the representative experimental stress vs. strain curves are shown in Fig. 4. A magenta straight line with a slope of one is given to reveal the deviation, less than 10%, of the predicted yield strength from the experimental one.**

method provides a close agreement with the experimental results (Fig. 5), a pioneering result from this work.

Through analyzing by employing HE-SXRD data and an analytical model, the YS of the present SDSS is understood to be mainly controlled by the grain refinement and the stored dislocations due to plastic deformation. This also indicates a correlation between the deformation modes, strain levels, and YS of SDSS. Despite the fact that complex microstructures can be developed in such SDSS after deformation [20–22], a combination of quick HE-SXRD measurement and analytical model can be applied to predict the microstructural features and corresponding YS after thermomechanical processing, which provides unique pathways for designing high strength steel prior to multiscale characterizations. Prediction of YS for single phase alloy is common to achieve, however, the same for multiphase steel is lacking. This work, on the other hand, benefits the idea of highly alloyed multiphase steels for the precise prediction of YS using composite type analytical model to estimate the exact contribution of different phases (austenite, ferrite/martensite, cementite, and precipitations, etc.).

#### 4. Conclusion

In summary, HE-SXRD experiments and an analytical model were employed to predict the yield strength of Ce-modified SDSS subjected to various cold- and cryo-deformation. In addition to microstructural details, HE-SXRD data identifies major as well as minor phases e.g.,  $\text{Cr}_2\text{N}$  and rare earth based eutectic phases. Implementation of complete structural informations in semi-empirical analytical model results in similar YS values as experimentally measured. Such close agreement of predicted results compared to measured ones

establishes a pioneer outcome obtained solely from HE-SXRD data. The following conclusions can be drawn from the present investigation:

- Clear differences in the relative intensities of various peaks of the major phases ( $\alpha/\alpha'$  and  $\gamma$ ) for the two different sources (LS-XRD and HE-XRD) are apparent. Several additional peaks correspond to secondary phases of  $\text{Cr}_2\text{N}$  and eutectic  $\text{Ce}_x\text{Fe}_y$  are not revealed through LS-XRD.
- The average lattice microstrain in austenite increased from  $4.7 \times 10^{-3}$  to  $7.2 \times 10^{-3}$  and in martensite increased from  $1.9 \times 10^{-3}$  and  $3.2 \times 10^{-3}$  with an increase in rolling reduction from 30 to 90% along with a concomitant decrease in the grain size from  $\sim 122$  to 82 nm and 113 to 61 nm, respectively. A similar trend was observed in the case of CGR specimen. A relatively higher level of microstrain within austenite as compared to ferrite/martensite phase could be attributed to the high strain hardening ability of austenite compared to ferrite/martensite.
- Among different strengthening mechanisms, grain size strengthening mechanism was found to play a pivotal role in high strength levels.
- Theoretical YS based on a unique composite strengthening model correlated well with experimentally evaluated yield strength.

Overall, this study provides new pathways for highly alloyed complex multiphase structural and engineering materials to predict the yield strength of steels which would help to design/engineer high strength steel by better understanding the relationship of individual phase properties to their mechanical response.

#### Data availability statement

All data included in this study are available upon request by contacting the corresponding author.

#### Credit authorship contribution statement

SG: Conceptualization, Methodology, Formal analysis, Data curation, Investigation, Writing; SW: LS- and HE-XRD data analysis, Data curation, Writing; HS: Synchrotron data collection, problem planning, conceptualization, methodology, review & editing; GK: Synchrotron data collection, review & editing; YX: Project initialization, funding acquisition, review & editing; TZ: Review & editing; MH, JK & WC: Supervision, Funding acquisition.

#### Declaration of Competing Interest

The authors declare that they have no known competing financial interests or personal relationships that could have appeared to influence the work reported in this paper.

## Acknowledgments

The authors heartily thank Prof. Pentti Karjalainen and Ass. Prof. Levente Balogh for their fruitful discussions. The authors acknowledge Academy of Finland grant No. #311934 for the financial support. The research described in this paper was performed at the Canadian Light Source, a national research facility of the University of Saskatchewan, which is supported by the Canada Foundation for Innovation (CFI), the Natural Sciences and Engineering Research Council (NSERC), the National Research Council (NRC), the Canadian Institutes of Health Research (CIHR), the Government of Saskatchewan, and the University of Saskatchewan. The Center for Materials Analysis, University of Oulu is also acknowledged for the in-house characterizations. The authors also acknowledge National Natural Science Foundation of China (# 51801054 and U1804146), Program for Science, Technology Innovation Talents in Universities of Henan Province (# 17HASTIT026), Science and Technology Innovation Team of Henan University of Science and Technology (# 2015XTD006), and Foreign Experts and Wisdom Introduction Program in Henan Province (# HNGD2020009) for the financial support.

## REFERENCES

- [1] Marques F, Da Silva WM, Pardal JM, Tavares SSM, Scandian C. Influence of heat treatments on the micro-abrasion wear resistance of a superduplex stainless steel. *Wear* 2011;271:1288–94. <https://doi.org/10.1016/j.wear.2010.12.087>.
- [2] Jia N, Cong ZH, Sun X, Cheng S, Nie ZH, Ren Y, et al. An in situ high-energy X-ray diffraction study of micromechanical behavior of multiple phases in advanced high-strength steels. *Acta Mater* 2009;57:3965–77. <https://doi.org/10.1016/j.actamat.2009.05.002>.
- [3] Jia N, Lin Peng R, Wang YD, Johansson S, Liaw PK. Micromechanical behavior and texture evolution of duplex stainless steel studied by neutron diffraction and self-consistent modeling. *Acta Mater* 2008;56:782–93. <https://doi.org/10.1016/j.actamat.2007.10.040>.
- [4] Cong ZH, Jia N, Sun X, Ren Y, Almer J, Wang YD. Stress and strain partitioning of ferrite and martensite during deformation. *Metall Mater Trans A* 2009;40:1383–7. <https://doi.org/10.1007/S11661-009-9824-2/FIGURES/7>.
- [5] Fu B, Yang WY, Wang YD, Li LF, Sun ZQ, Ren Y. Micromechanical behavior of TRIP-assisted multiphase steels studied with in situ high-energy X-ray diffraction. *Acta Mater* 2014;76:342–54. <https://doi.org/10.1016/j.actamat.2014.05.029>.
- [6] Zhang Z, Tan Q, Cui Y, Tian Y, Wang Y, Qin H, et al. Experimental validation of residual stress thermomechanical simulation in as-quenched superalloy discs by using diffraction and incremental hole-drilling methods. *Mater Today Commun* 2021;27:102229. <https://doi.org/10.1016/j.mtcomm.2021.102229>.
- [7] Galindo-Nava EI, Rainforth WM, Rivera-Díaz-del-Castillo PEJ. Predicting microstructure and strength of maraging steels: elemental optimisation. *Acta Mater* 2016;117:270–85. <https://doi.org/10.1016/j.actamat.2016.07.020>.
- [8] Wang JS, Mulholland MD, Olson GB, Seidman DN. Prediction of the yield strength of a secondary-hardening steel. *Acta Mater* 2013;61:4939–52. <https://doi.org/10.1016/j.actamat.2013.04.052>.
- [9] Seol JB, Raabe D, Choi PP, Im YR, Park CG. Atomic scale effects of alloying, partitioning, solute drag and austempering on the mechanical properties of high-carbon bainitic-austenitic TRIP steels. *Acta Mater* 2012;60:6183–99. <https://doi.org/10.1016/j.actamat.2012.07.064>.
- [10] Wang H, Li Y, Detemple E, Eggeler G. Revealing the two-step nucleation and growth mechanism of vanadium carbonitrides in microalloyed steels. *Scripta Mater* 2020;187:350–4. <https://doi.org/10.1016/j.scriptamat.2020.06.041>.
- [11] Qian F, Sharp J, Rainforth WM. Microstructural evolution of Mn-based maraging steels and their influences on mechanical properties. *Mater Sci Eng* 2016;674:286–98. <https://doi.org/10.1016/j.msea.2016.08.006>.
- [12] Lee S, Lee SJ, De Cooman BC. Austenite stability of ultrafine-grained transformation-induced plasticity steel with Mn partitioning. *Scripta Mater* 2011;65:225–8. <https://doi.org/10.1016/j.scriptamat.2011.04.010>.
- [13] Peeters B, Bacroix B, Teodosiu C, Van Houtte P, Aernoudt E. Work-hardening/softening behaviour of b.c.c. polycrystals during changing strain paths: II. TEM observations of dislocation sheets in an IF steel during two-stage strain paths and their representation in terms of dislocation densities. *Acta Mater* 2001;49:1621–32. [https://doi.org/10.1016/S1359-6454\(01\)00067-2](https://doi.org/10.1016/S1359-6454(01)00067-2).
- [14] Feng Z, Fu R, Lin C, Wu G, Huang T, Zhang L, et al. TEM-based dislocation tomography: challenges and opportunities. *Curr Opin Solid State Mater Sci* 2020;24:100833. <https://doi.org/10.1016/j.cossms.2020.100833>.
- [15] Li R, Tan Q, Wang Y, Yan Z, Ma Z, Wang YD. Grain-orientation-dependent phase transformation kinetics in austenitic stainless steel under low-temperature uniaxial loading. *Materialia (Oxf)* 2021;15:101030. <https://doi.org/10.1016/j.mtla.2021.101030>.
- [16] Li S, Wen P, Li S, Song W, Wang Y, Luo H. A novel medium-Mn steel with superior mechanical properties and marginal oxidization after press hardening. *Acta Mater* 2021;205:116567. <https://doi.org/10.1016/j.actamat.2020.116567>.
- [17] Esin VA, Denand B, Le Bihan Q, Dehmas M, Teixeira J, Geandier G, et al. In situ synchrotron X-ray diffraction and dilatometric study of austenite formation in a multi-component steel: influence of initial microstructure and heating rate. *Acta Mater* 2014;80:118–31. <https://doi.org/10.1016/j.actamat.2014.07.042>.
- [18] Wang YQ, Clark SJ, Janik V, Heenan RK, Venero DA, Yan K, et al. Investigating nano-precipitation in a V-containing HSLA steel using small angle neutron scattering. *Acta Mater* 2018;145:84–96. <https://doi.org/10.1016/j.actamat.2017.11.032>.
- [19] Zhang M, Li L, Ding J, Wu Q, Wang YD, Almer J, et al. Temperature-dependent micromechanical behavior of medium-Mn transformation-induced-plasticity steel studied by in situ synchrotron X-ray diffraction. *Acta Mater* 2017;141:294–303. <https://doi.org/10.1016/j.actamat.2017.09.030>.
- [20] Zhou T, Xiong Y, Yue Y, Lu Y, Chen Y na, He T tian, et al. Controlled cold rolling effect on microstructure and mechanical properties of Ce-modified SAF 2507 super duplex stainless steel. *Mater Sci Eng* 2019;766:138352. <https://doi.org/10.1016/j.msea.2019.138352>.
- [21] Zhou T, Xiong Y, Zha X, Lu Y, He T, Ren F, et al. Microstructural evolution induced mechanical property enhancement in cryogenically rolled Ce-modified SAF2507 super duplex stainless steel. *Adv Eng Mater*

- 2020;2000516:2000516. <https://doi.org/10.1002/adem.202000516>.
- [22] Zhou T, Xiong Y, Zha X, Yue Y, Lu Y, He T, et al. Hot-deformation-induced structural and mechanical properties of Ce-modified SAF 2507 super duplex stainless steel. *J Mater Res Technol* 2020;9:8379–90. <https://doi.org/10.1016/j.jmrt.2020.05.123>.
- [23] Toby BH, Von Dreele RB. GSAS-II: the genesis of a modern open-source all purpose crystallography software package. *J Appl Crystallogr* 2013;46:544–9. <https://doi.org/10.1107/S0021889813003531>.
- [24] Dr. H. Putz, Dr. K. Brandenburg GbR. Match! - Phase Analysis using Powder Diffraction. <https://www.crystalimpact.de/match>.
- [25] Mote V, Purushotham Y, Dole B. Williamson-Hall analysis in estimation of lattice strain in nanometer-sized ZnO particles. *Journal of Theoretical and Applied Physics* 2012;6:1–8. <https://doi.org/10.1186/2251-7235-6-6>.
- [26] Williamson GK, Smallman III RE. Dislocation densities in some annealed and cold-worked metals from measurements on the X-ray Debye-Scherrer spectrum. *Phil Mag* 1956;1:34–46. <https://doi.org/10.1080/14786435608238074>.
- [27] El-Tahawy M, Huang Y, Um T, Choe H, Lábár JL, Langdon TG, et al. Stored energy in ultrafine-grained 316L stainless steel processed by high-pressure torsion. *J Mater Res Technol* 2017;6:339–47. <https://doi.org/10.1016/j.jmrt.2017.05.001>.
- [28] Funakawa Y, Shiozaki T, Tomita K, Yamamoto T, Maeda E. Development of high strength hot-rolled sheet steel consisting of ferrite and nanometer-sized carbides. *ISIJ Int* 2004;44:1945–51. <https://doi.org/10.2355/isijinternational.44.1945>.
- [29] Raabe D. Texture and microstructure evolution during cold rolling of a strip cast and of a hot rolled austenitic stainless steel. *Acta Mater* 1997;45:1137–51. [https://doi.org/10.1016/S1359-6454\(96\)00222-4](https://doi.org/10.1016/S1359-6454(96)00222-4).
- [30] Raabe D, Lücke K. Texture and microstructure of hot rolled steel. *Scripta Metall Mater* 1992;26:1221–6. [https://doi.org/10.1016/0956-716X\(92\)90567-X](https://doi.org/10.1016/0956-716X(92)90567-X).
- [31] Mulholland MD, Seidman DN. Multiple dispersed phases in a high-strength low-carbon steel: an atom-probe tomographic and synchrotron X-ray diffraction study. *Scripta Mater* 2009;60:992–5. <https://doi.org/10.1016/j.scriptamat.2009.02.033>.
- [32] Dutta RK, Huizenga RM, Amirthalingam M, King A, Gao H, Hermans MJM, et al. In situ synchrotron diffraction studies on the temperature-dependent plane-specific elastic constants in a high-strength quenched and tempered structural steel. *Scripta Mater* 2013;69:187–90. <https://doi.org/10.1016/j.scriptamat.2013.03.031>.
- [33] Li M, Yin T, Wang Y, Du F, Zou X, Gregersen H, et al. Study of biocompatibility of medical grade high nitrogen nickel-free austenitic stainless steel in vitro. *Mater Sci Eng C* 2014;43:641–8. <https://doi.org/10.1016/j.msec.2014.06.038>.
- [34] Wang H, Bao Y ping, Zhao M, Wang M, Yuan X ming, Gao S. Effect of Ce on the cleanliness, microstructure and mechanical properties of high strength low alloy steel Q690E in industrial production process. *International Journal of Minerals, Metallurgy and Materials* 2019;26:1372–84. <https://doi.org/10.1007/s12613-019-1871-0>.
- [35] Lin Q, Guo F, Zhu X. Behaviors of lanthanum and cerium on grain boundaries in carbon manganese clean steel. *J Rare Earths* 2007;25:485–9. [https://doi.org/10.1016/S1002-0721\(07\)60461-X](https://doi.org/10.1016/S1002-0721(07)60461-X).
- [36] Singh H, Alatarvas T, Kistanov AA, Aravindh SA, Wang S, Zhu L, et al. Unveiling interactions of non-metallic inclusions within advanced ultra-high-strength steel: a spectro-microscopic determination and first-principles elucidation. *Scripta Mater* 2021;197:113791. <https://doi.org/10.1016/j.scriptamat.2021.113791>.
- [37] Singh H, Xiong Y, Rani E, Wang S, Kharbach M, Zhou T, et al. Unveiling nano-scaled chemical inhomogeneity impacts on corrosion of Ce-modified 2507 super-duplex stainless steels. *npj Mater Degrad* 2022;6:54. <https://doi.org/10.1038/s41529-022-00263-z>.
- [38] Zhang L, Song R, Zhao C, Yang F. Work hardening behavior involving the substructural evolution of an austenite-ferrite Fe-Mn-Al-C steel. *Mater Sci Eng* 2015;640:225–34. <https://doi.org/10.1016/j.msea.2015.05.108>.
- [39] Ghosh S, Bibhanshu N, Suwas S, Chatterjee K. Surface mechanical attrition treatment of additively manufactured 316L stainless steel yields gradient nanostructure with superior strength and ductility. *Mater Sci Eng, A* 2021;820:141540. <https://doi.org/10.1016/j.MSEA.2021.141540>.
- [40] Hansen N. Hall-petch relation and boundary strengthening. *Scripta Mater* 2004;51:801–6. <https://doi.org/10.1016/j.scriptamat.2004.06.002>.
- [41] Zhang X, Hansen N, Gao Y, Huang X. Hall-Petch and dislocation strengthening in graded nanostructured steel. *Acta Mater* 2012;60:5933–43. <https://doi.org/10.1016/j.actamat.2012.07.037>.
- [42] Ghosh S, Mula S. Improvement of fracture toughness of Ti+Nb stabilized microalloyed and interstitial free steels processed through single phase regime control multiaxial forging. *Mater Sci Eng* 2020;772:138817. <https://doi.org/10.1016/j.msea.2019.138817>.
- [43] Ghosh S, Singh AK, Mula S. Effect of critical temperatures on microstructures and mechanical properties of Nb-Ti stabilized IF steel processed by multiaxial forging. *Mater Des* 2016;100:47–57. <https://doi.org/10.1016/j.matdes.2016.03.107>.
- [44] Cottrell AH. Dislocations and the mechanical properties of crystals. *Nature* 1956;178:1090–2.
- [45] Gladman T. Precipitation hardening in metals. *Mater Sci Technol* 1999;15:30–6. <https://doi.org/10.1179/026708399773002782>.
- [46] Maropoulos S, Paul JDH, Ridley N. Microstructure–property relationships in tempered low alloy Cr–Mo–3.5Ni–V steel. *Mater Sci Technol* 1993;9:1014–20. <https://doi.org/10.1179/mst.1993.9.11.1014>.
- [47] HajyAkbari F, Sietsma J, Böttger AJ, Santofimia MJ. An improved X-ray diffraction analysis method to characterize dislocation density in lath martensitic structures. *Mater Sci Eng, A* 2015;639:208–18. <https://doi.org/10.1016/j.msea.2015.05.003>.
- [48] Ungár T, Ott S, Sanders PG, Borbély A, Weertman JR. Dislocations, grain size and planar faults in nanostructured copper determined by high resolution X-ray diffraction and a new procedure of peak profile analysis. *Acta Mater* 1998;46:3693–9. [https://doi.org/10.1016/S1359-6454\(98\)00001-9](https://doi.org/10.1016/S1359-6454(98)00001-9).
- [49] Hashemi J, Presuel-Moreno F. *Foundations of materials science and engineering*. 2019.
- [50] Liang ZY, Li YZ, Huang MX. The respective hardening contributions of dislocations and twins to the flow stress of a twinning-induced plasticity steel. *Scripta Mater* 2016;112:28–31. <https://doi.org/10.1016/j.scriptamat.2015.09.003>.